Supplemental Material

A comparison of atmospheric CO_2 flux signals obtained from GEOSChem flux inversions constrained by in situ or GOSAT observations

Saroja M. Polavarapu[1], Feng Deng[2], Brendan Byrne[2], Dylan B. Jones[2], Michael Neish[1]

Estimating uncertainty in CO_2 simulations due to the presence of meteorological uncertainty

In this section we describe the method used to produce perturbations of meteorological analyses. The perturbed and unperturbed meteorological fields are used with posterior fluxes in two parallel simulations of CO_2. The difference between the 4-dimensional CO_2 fields resulting from the two simulations quantifies the impact of uncertain winds on the CO_2 simulation. In Polavarapu et al. (2016), the perturbation was obtained by computing the difference in analyses valid 6 h apart and removing the diurnal signal (by subtracting the monthly mean of each synoptic hour from each perturbation). As noted in that article, this was used as a "proxy" for analysis error because while ECCC has an operational ensemble Kalman Filter (EnKF) for ensemble prediction (Houtekamer et al. 2014) and hence estimates of analysis error, the ensemble members archived at the Canadian Meteorological Centre only begin in 2011, and only become reliable in 2012. In this work, we use an actual realization of analysis error from the archived CMC ensemble perturbations from 2012 because (as will be shown below) the difference between proxy and actual ensemble perturbations is much greater than the error incurred by using the wrong year for the ensemble perturbation.

The analysis errors were computed for the year 2010 at 24 h frequency. The proxy analysis error was computed as described above. For the ensemble perturbation, the EnKF which was operational in 2012 used 192 members and thus 192 possible perturbations can be obtained by subtracting each member from the ensemble mean. Since the full year integration of analysis error for just 1 member already requires 2 year-long integrations (one with control meteorology, the second with perturbed meteorology) which are computationally expensive, it would be very difficult to consider even a few members. However, once our full EnKF including greenhouse gas estimation which is under development is completed, we will have exactly this capability. Until then, we must choose a single ensemble member for practical reasons. Theoretically, this is justifiable because the ensemble members are supposed to be equally-likely realizations of analysis error, and this can be verified using rank histograms (Hamill 2001, Houtekamer and Zhang 2016). Nevertheless, we also show below that the impact of choosing a different ensemble member is small compared to using the proxy analysis error in place of an EnKF estimated error.

To encapsulate the two types of analysis error realizations which are 4-dimensional fields available for a full year, we compute some 2-dimensional diagnostics. First we compute 3-dimensional

monthly mean errors. Then, the zonal mean and zonal standard deviations of the monthly means were computed and are shown in Figure S1 for the month of July. Specifically, July 2010 is used for the proxy error but July 2012 is used for the ensemble perturbation based on member 2 of 192. (The impact of using the wrong year for the ensemble perturbation will be discussed shortly.) First note that, by design, the monthly mean proxy error is zero because we removed the diurnal signal (by subtracting the monthly mean perturbation). The ensemble perturbation has no such constraint and thus a zonal mean signal is present, with largest amplitude in the tropical stratosphere (second panel). Ensemble perturbations in the ECCC system are intended to represent model errors and are computed by perturbing aspects of the model which are known to have the largest uncertainty. Specifically, parameters in the boundary layer, deep convection, etc. are varied using an option table with each option having at least 2 possible values. Each member uses a unique combination of the 10 traits in the option table. Given that the greatest uncertainty in our model's forecasts is associated with physical parameterizations, particularly, those associated with tropical convection, the pattern in Figure S1 is not surprising. Any perturbation applied to tropical convection in the troposphere will impact the generation of tropical waves which propagate up to the stratosphere, impacting the zonal mean flow and signals such as the quasi-biennial oscillation (QBO). The variability of the 4D errors about the zonal mean is described by the zonal standard deviation diagnostic. Here we see rather different patterns for the two types of errors. For the proxy error (Figure S1, third panel), the tropospheric jets are evident. This occurs because a difference in atmospheric states taken 6 h apart reflects true changes in the state. In particular, large wind speeds in the jet stream will produce large temporal differences. The true atmospheric change in 6 h should not be included in analysis error, so this pattern is not desirable. The error in the upper stratosphere is likely also related to the large wind speeds found there. The fourth panel shows the ensemble-based analysis error zonal standard deviation is largest in the tropical stratosphere. This means that not just the zonal mean but the zonal anomalies are large there. This is consistent with the notion that differences in zonal wave spectra between the control and perturbed simulations arise because model perturbations impact the spectrum of tropical waves generated in the forecast. In summary, Figure S1 shows that the proxy error obtained by differencing two analysis states (and removing the diurnal signal) is very different qualitatively from an actual realization of analysis error from our system. Similar figures were produced for meridional wind and temperature fields but are not shown as they were qualitatively similar to Figure S1.

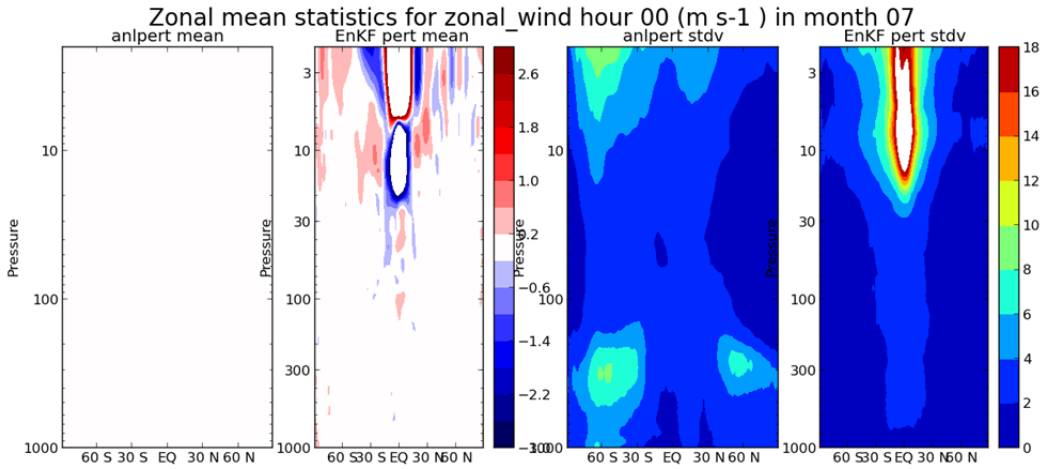

Figure S1. Zonal mean statistics for the proxy and ensemble-based analysis errors as a function of pressure and latitude. The zonal mean is shown in the left two panels with the same colour bar, while the zonal standard deviation is shown in the right two panels, with the colour bar on the right. Units are ms^{-1}. The proxy error statistics are found in the first and third panels while the EnKF analysis error statistics are found in the second and fourth panels.

Given that actual ensemble error realizations are preferable to the proxy used in Polavarapu et al. (2016) yet are unavailable for the time period of interest, we examine how much the ensemble perturbations vary with the year. Over time, in an operational assimilation system, components of the system are continually updated. We shall compare the ensemble perturbation based on member 2 for 2014 and 2012. Between these two dates, a number of improvements were made in two major updates. These changes are as follows. On 13 February 2013, the horizontal grid of the model was changed from 200x400 to 300x600 grid points and the vertical levels increased from 58 to 74. The model physics was changed also. More satellite data were added (from AMSU) and bias correction algorithms were modified. On 4 December 2013, the model version changed again, more satellite data was assimilated and the sea surface temperature treatment changed. Thus, the operational ensemble prediction system changed considerably between 2012 and 2014. Figure S2 encapsulates the monthly analysis errors for July 2012 (top row) and July 2014 (bottom row) for temperature, zonal and meridional wind and specific humidity in 1-dimensional profiles which are area weighted global means of zonal statistics. For reference, comparable diagnostics for the proxy error are also shown as dashed curves. Below 30 hPa, the ensemble perturbation statistics are very similar for the two years (compare solid lines in upper and lower rows). The biggest differences occur above 30 hPa, but even there, the 2012 and 2014 ensemble perturbations are more similar to each other than to the proxy error.

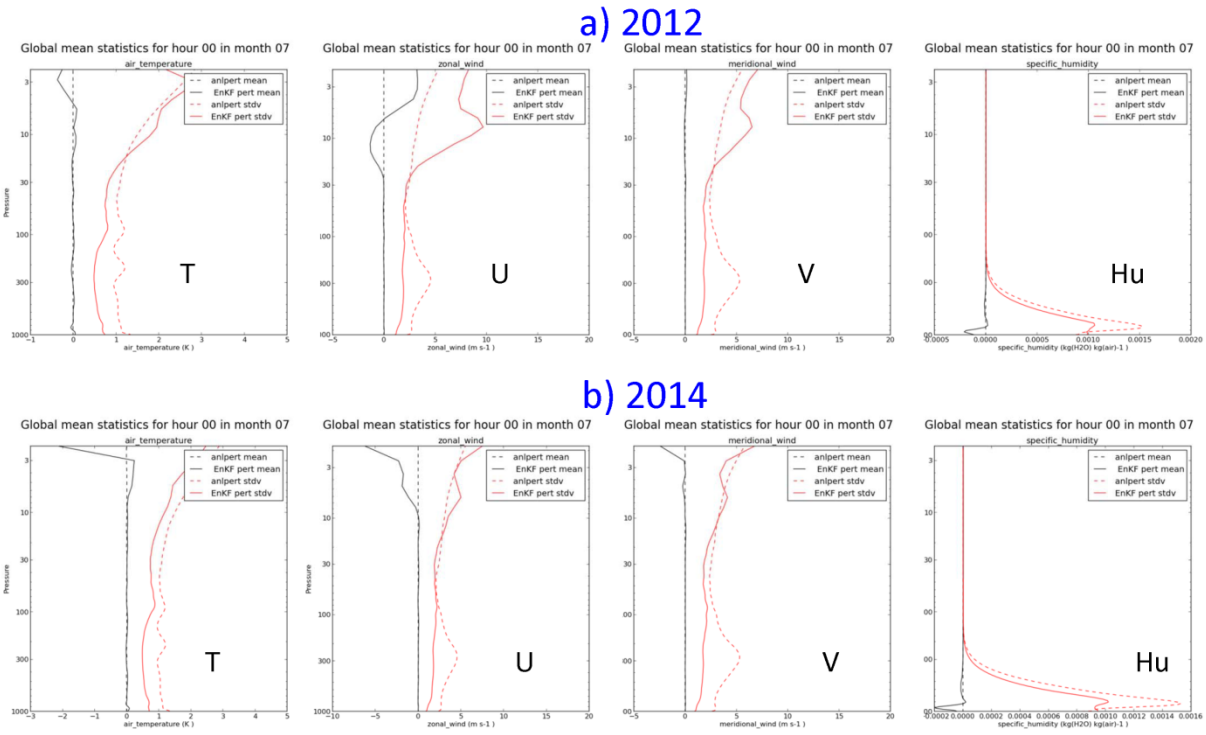

Figure S2. Change in ensemble perturbation as a function of year. Monthly means of analysis error are produced then zonal mean and zonal standard deviations are computed. The global means of the zonal mean (black curves) and zonal standard (red curves) deviation are shown here for the ensemble Kalman Filter perturbation based on member 2 (solid curves) for a) July 2012 and b) July 2014. Units are K for temperature and ms^{-1} for zonal wind. Also shown, for reference, are comparable curves for the proxy error (dashed lines) which are identical for a given variable in upper and lower panels.

A spatial depiction of analysis errors is presented in Figure S3 which presents surface pressure statistics for July. Comparing left and right columns reveals significant differences between the two methods of estimating analysis errors. The proxy error picks up on the large wind speeds in the southern hemisphere winter in the “roaring 40s”. Again, this occurs because the 6 h difference includes the true change in atmospheric states in 6 h (which it should not). This is not seen in the ensemble Kalman filter estimate. Furthermore, the difference in perturbations between the two years (compare top 4 and bottom 4 panels) is small compared to the difference in analysis error type.

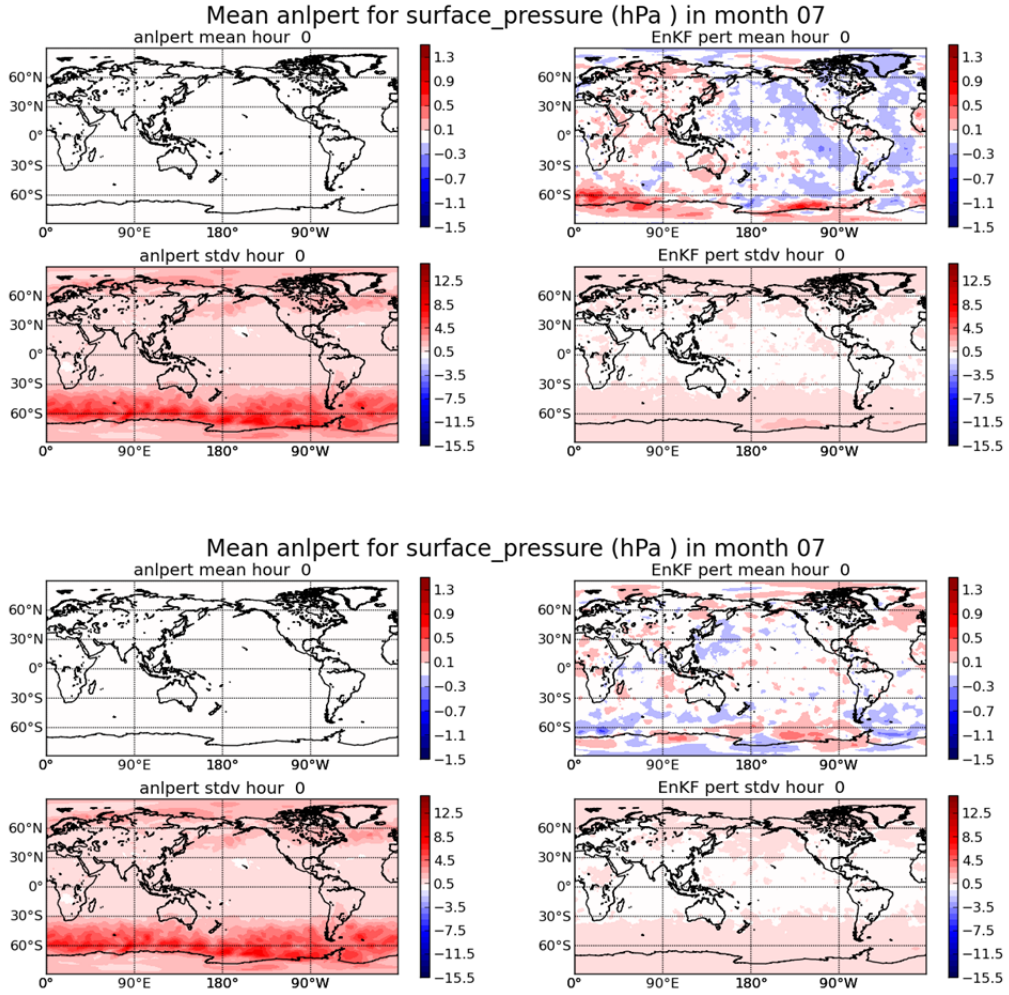

Figure S3. Monthly mean analysis error for surface pressure for July. Each set of four panels are for mean errors (top rows) or standard deviation about the time mean (bottom rows) at hour 0 for the proxy error (left columns) or the ensemble Kalman Filter estimate (right columns) based on member 2. The top 4 panels are for 2012 while the bottom 4 are for 2014. Note that the proxy errors are the same in the top set of 4 and the bottom set of 4 panels and correspond to 2010.

To consider the impact of arbitrarily choosing one of 192 ensemble members, we compare the ensemble error estimates from members 2, 9 and 123. The biggest differences are found in the zonal wind field above 10hPa (most diagnostics not shown). The zonal statistics for the July mean error are shown in Figure S4. It is evident that the choice of ensemble member is far less important than choosing the EnKF estimate over the proxy error.

We also considered the variation of ensemble perturbations with season by comparing perturbations in January and July 2012. The biggest differences are found in the zonal wind monthly mean errors above 10 hPa in terms of the zonal mean (Figure S5). Once again, we can conclude that the variation with season of the ensemble Kalman filter analysis error is not significant compared to choosing the EnKF estimate over the proxy estimate. Nevertheless, to keep some seasonal variation while minimizing storage space and computational needs, ensemble perturbations are computed for each month based on January, April, July and October. That is, January perturbations are applied to December and

February as well as to January fields. The same process applies for the other months. In the end, analysis error perturbations based on member 2 were produced for 2010 using the 2012 perturbations for each day of the year. The same perturbations (for the appropriate month) were also applied in the second half of 2009 and in the first half of 2011.

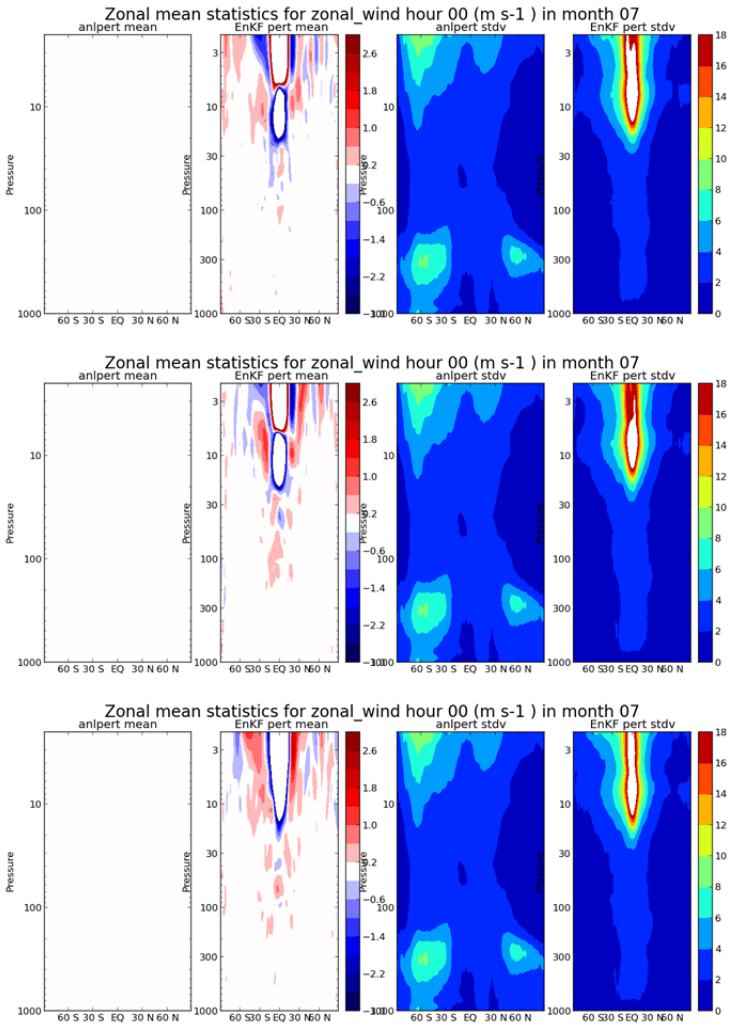

Figure S4. Zonal mean statistics for the proxy and ensemble-based analysis errors as a function of pressure and latitude. Ensemble member2 is shown in the top row, member 9 in the middle row and member 123 in the bottom row. The zonal mean is shown in the left two panels, while the zonal standard deviation is shown in the right two panels. Note that the proxy error panels are identical in all rows.

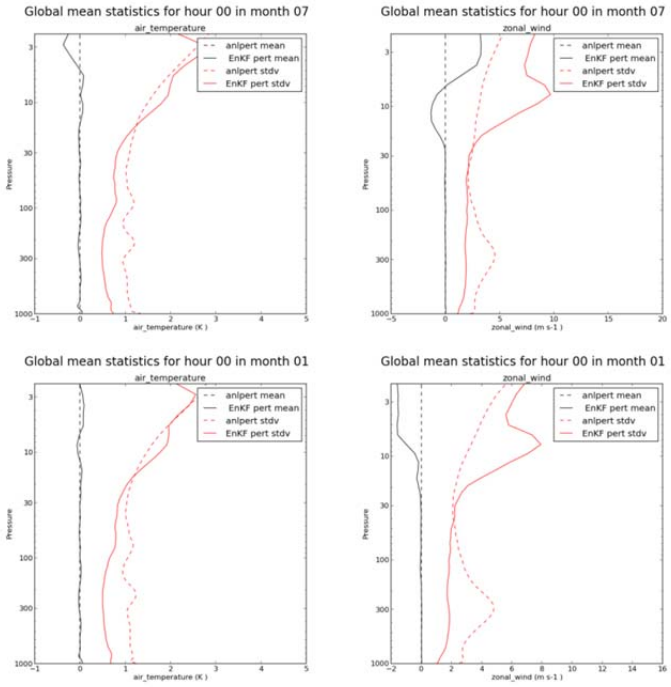

Figure S5. Change in ensemble error estimate as a function of season. Monthly means of analysis error are produced, then zonal mean and zonal standard deviations are computed. The global means of the zonal mean (black curves) and zonal standard (red curves) deviation are shown here for the ensemble Kalman Filter perturbation based on member 2 (solid curves) for July 2012 (top row) January 2012 (bottom row) for temperature (left column) and zonal wind (right column). Units are K for temperature and ms^{-1} for zonal wind. Also shown, for reference, are comparable curves for the proxy error (dashed lines) which are identical for a given variable in upper and lower panels.

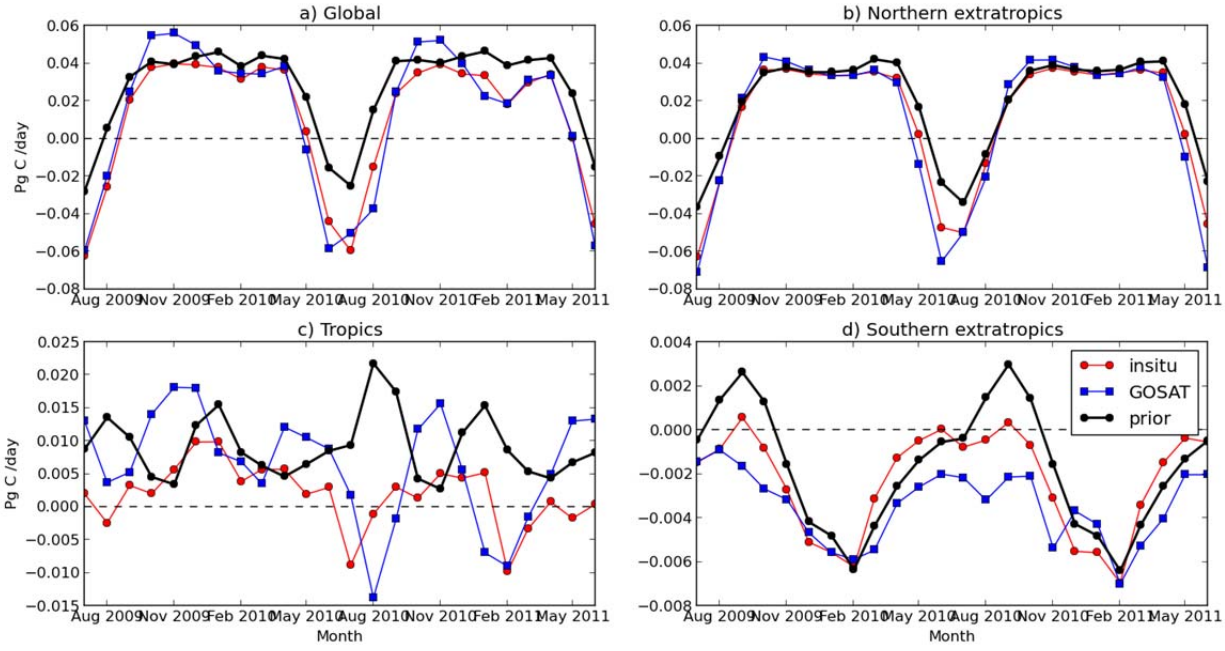

Figure S6. Prior and posterior fluxes area weighted and regionally averaged over (a) the whole globe, (b) the northern extratropics, (c) the tropics and (d) the southern extratropics. Fluxes are monthly averages from July 2009 to June 2011. Note the expanded vertical scales for panels c and d.

To see animation, open the file: geoschem_insitu-pri_vs_gosat-pri_2009-11_zonal_diffCO2.avi

Figure S7. Animation of a pair of differences in zonal mean CO_2 fields with GEOS-Chem. Zonal mean fields are displayed as a function height and latitude in units of ppm. The difference of the zonal mean CO_2 from the insitu posterior flux integration minus the prior flux integration (leftmost of the pair) is shown versus that from the GOSAT posterior flux integration minus the prior flux integration (rightmost of the pair).

To see animation, open the file: geoschem-vs-gem_gosat-pri_2009-11_zonal_diffCO2.avi

Figure S8. Animation of a pair of differences in zonal mean CO_2 fields. Zonal mean fields are displayed as a function height and latitude in units of ppm. The difference of the zonal mean CO_2 from the GOSAT posterior flux integration minus the prior flux integration is shown for the GEOS-Chem model (left panel) and for the GEM-MACH-GHG (right panel) model.

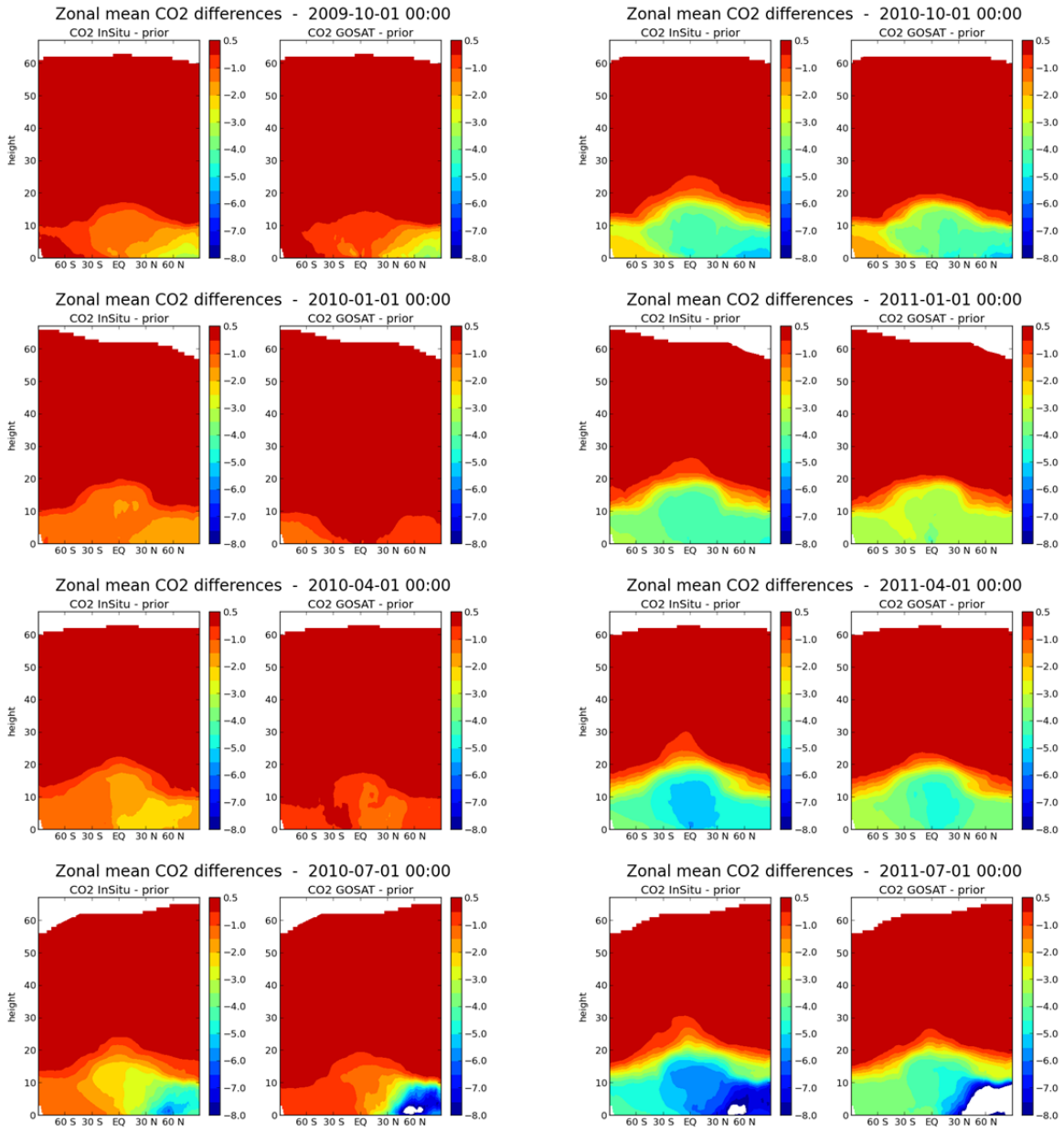

Figure S9. Time sequence of pairs of differences in zonal mean GEM CO_2 fields. Zonal mean fields are displayed as a function height and latitude in units of ppm. The difference of the zonal mean CO_2 from the insitu posterior flux integration minus the prior flux integration (leftmost of the pair) is shown versus that from the GOSAT posterior flux integration minus the prior flux integration (rightmost of the pair). The earliest date is in the top left corner with subsequent dates following down the left side then continuing down the right side. Dates are indicated above each pair of panels starting on 1 October 2009 and continuing in 3 month intervals to 1 July 2011.

Table S1: Comparison of GEOS-Chem and GEM-MACH-GHG CO_2 to TCCON observations. The 6-season averaged seasonal means from Figure 9 are given in columns 2-4. These averages are also plotted in Figures 8 and S10. The mean absolute departures of seasonal means from this time average are shown in columns 5-7. This statistic is a measure of the "flatness" of the curves seen in each panel of Figures 9 and S11. The total numbers of observations used in the statistics for each station are given in column 8. For each statistic, the top value corresponds to the GEM-MACH-GHG results with bottom corresponding to the GEOS-Chem results. Two different instruments are Lauder are used.

Station	<prior>	<in situ>	<GOSAT>	<|prior'|>	<|in situ'|>	<|GOSAT'|>	No. obs
Lauder 1	3.02	0.78	1.30	0.99	0.19	0.17	424
	2.46	0.22	0.70	0.96	0.13	0.20	
Lauder 2	3.30	0.90	1.58	1.27	0.19	0.15	1280
	2.67	0.30	0.89	1.34	0.23	0.17	
Wollongong	3.52	0.99	1.60	1.28	0.29	0.33	1269
	3.00	0.46	1.00	1.35	0.30	0.40	
Darwin	4.02	0.74	1.36	1.11	0.13	0.18	536
	3.46	0.23	0.82	1.09	0.09	0.18	
Izana	3.31	0.17	0.82	0.98	0.57	0.56	211
	3.49	0.21	0.84	1.04	0.28	0.21	
Lamont	2.98	-0.21	0.39	0.90	0.53	0.44	3087
	3.03	-0.22	0.29	0.99	0.45	0.25	
Park Falls	3.26	0.03	0.61	1.57	0.65	0.33	1662
	3.38	-0.03	0.60	1.58	0.56	0.29	
Garmich	3.16	-0.05	0.57	1.55	0.77	0.52	1172
	4.25	0.72	1.36	1.26	0.35	0.27	
Orleans	3.72	0.30	0.90	1.49	0.71	0.45	674
	3.58	0.04	0.68	1.57	0.78	0.48	
Karlsruhe	4.83	1.02	1.55	0.74	0.41	0.24	663
	4.85	0.88	1.44	0.68	0.40	0.20	
Bremen	3.75	0.42	0.99	1.11	0.31	0.24	278
	3.75	0.31	0.92	1.05	0.24	0.27	
Bialystok	3.36	0.09	0.68	0.93	0.57	0.29	858
	3.76	0.31	0.95	0.74	0.51	0.41	
Sodankyla	4.18	0.79	1.23	1.31	0.47	0.34	1188
	4.47	0.92	1.43	1.23	0.52	0.29	
Eureka	3.25	-1.19	-1.27	0.63	0.64	0.72	182
	3.56	-1.01	-0.94	0.62	0.63	0.68	

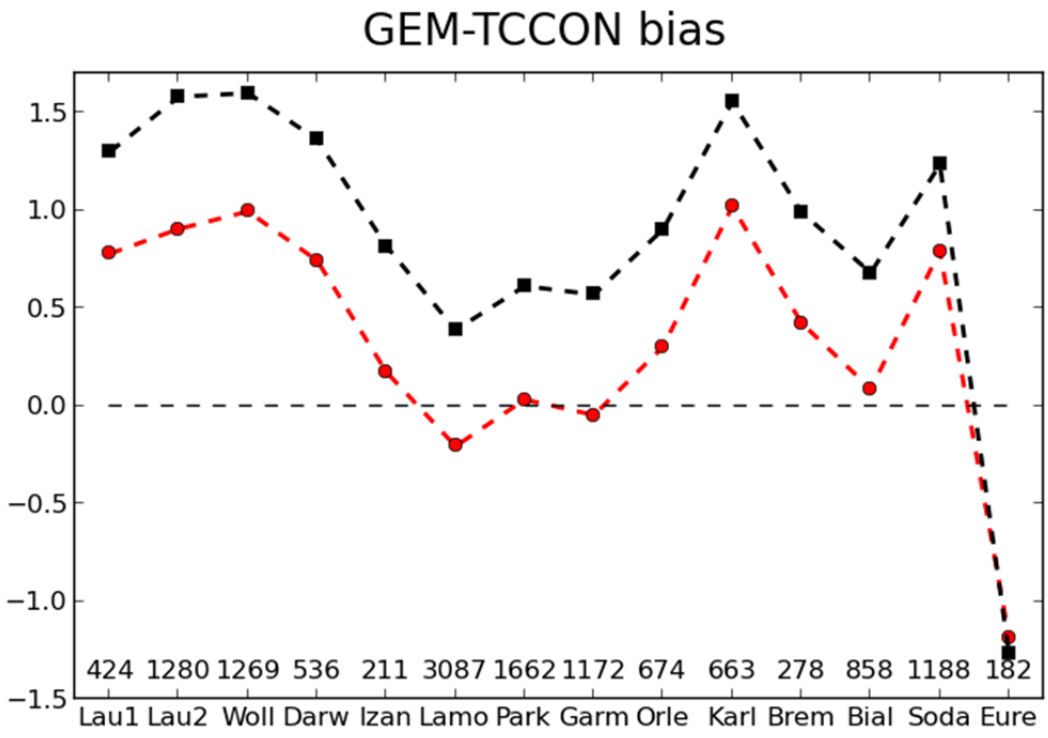

Figure S10. Comparison of GEM CO_2 simulations with GOSAT-derived (black) and in situ (red) derived posterior fluxes to TCCON measurements at 14 sites. First, the mean residual was computed for each station for each 3-month season and plotted in Figure S11. Then the 6 seasonal means (from each panel in Figure S11) were averaged.

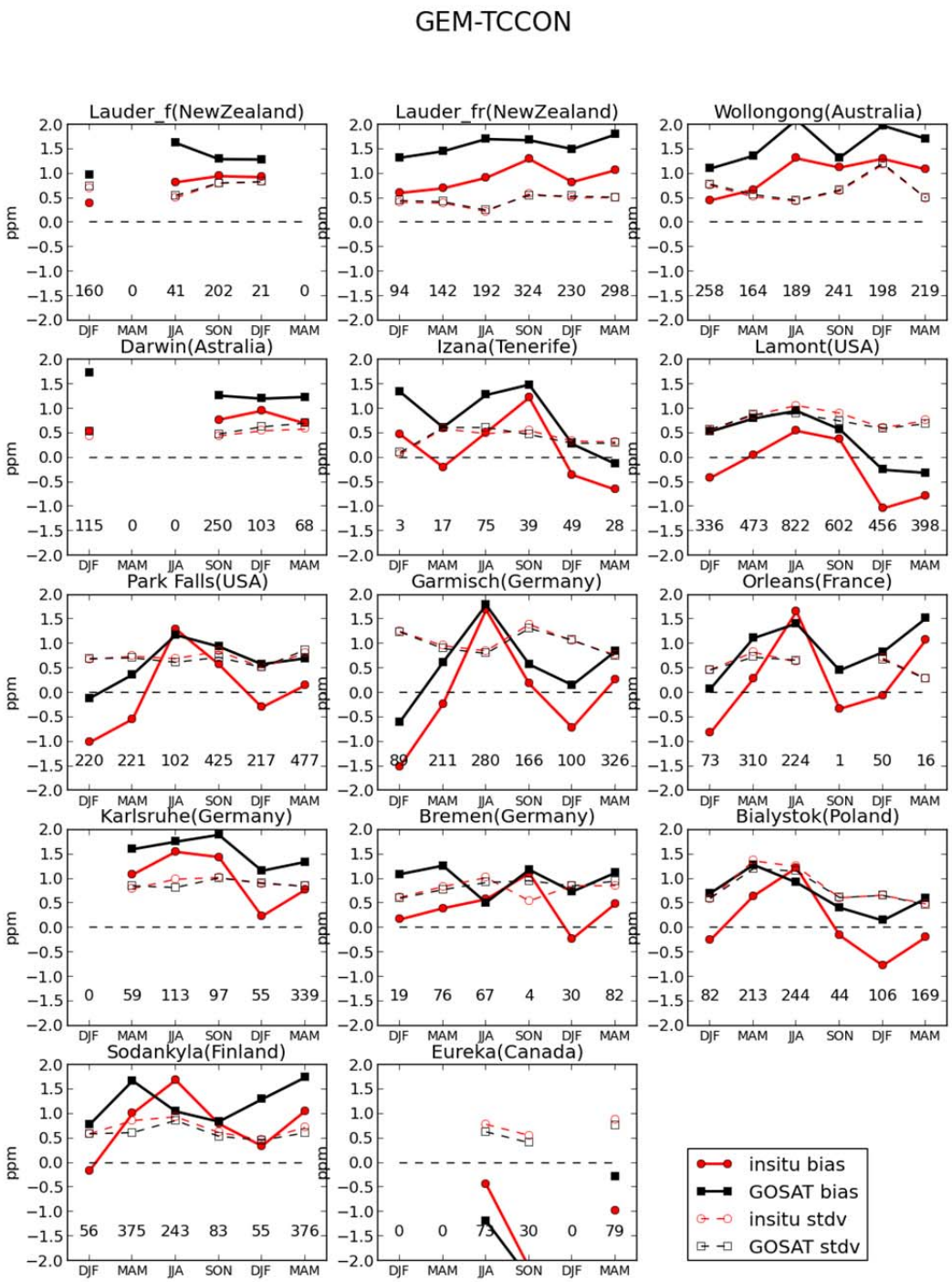

Figure S11. Comparison of GEM-MACH-GHG CO_2 simulations with GOSAT-derived (black) and in situ (red) derived posterior fluxes to TCCON measurements at 14 sites. Scores (bias and standard deviation) are aggregated by 3 month seasons from December 2009 to May 2011.

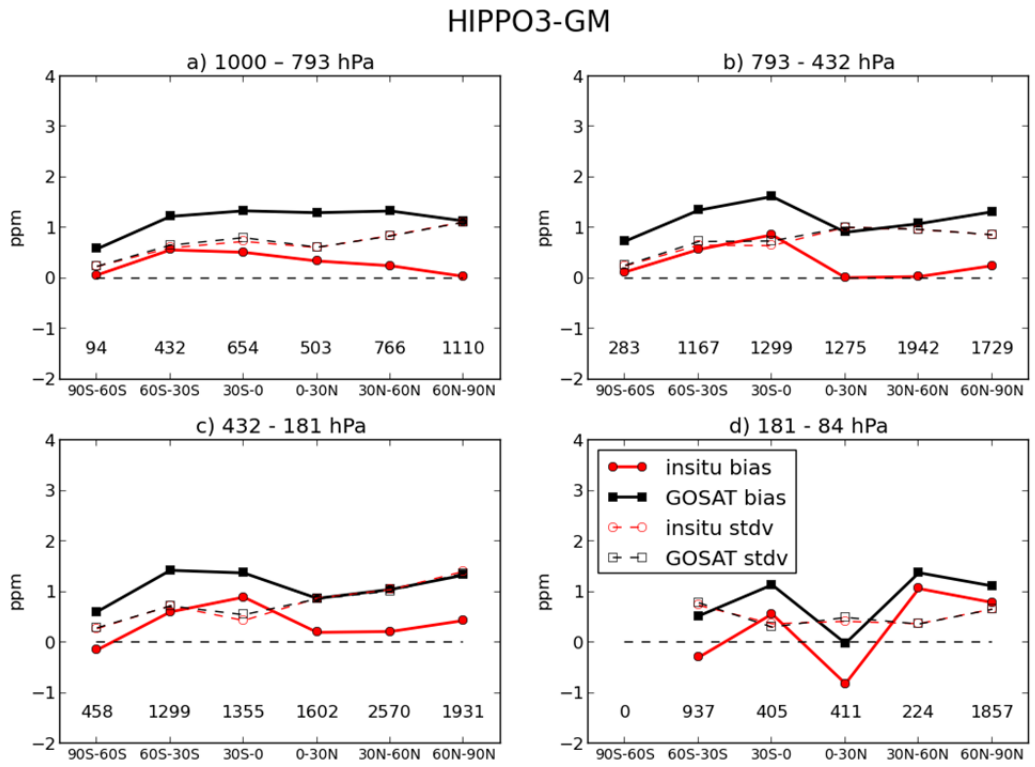

Figure S12. Comparison of GEM-MACH-GHG CO_2 simulations with GOSAT-derived (black) and in situ (red) derived posterior fluxes with HIPPO3 measurements. Scores (bias and standard deviation) of modelled minus observed values are aggregated by latitude band and over the pressure layers given above each panel. The numbers of observations used in each statistic are indicated within each panel. The flights occurred during 24 March to 16 April 2010.

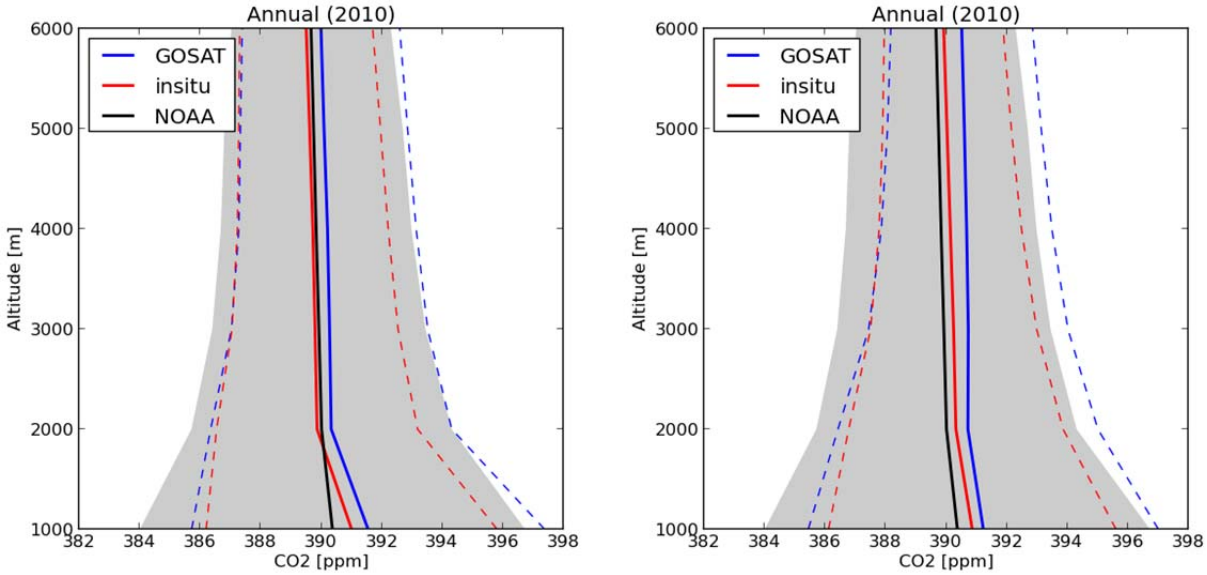

Figure S13. Comparison of mean GEOS-Chem (left) and GEM-MACH-GHG (right) model profiles of CO_2 to NOAA aircraft observations during 2010. Observations (black curves) are from obspack_co2_1_PROTOTYPE_v1.0.4_2013-11-25 for locations over continental U.S. and Canada, only. Model simulations used posterior fluxes from GEOS-Chem inversions with GOSAT (blue) or in situ (red) observations. The shaded grey regions indicate plus or minus one standard deviation for the observations while the dashed coloured lines indicate the same quantities but for the different model runs. Sites used are indicated in Figure 10.

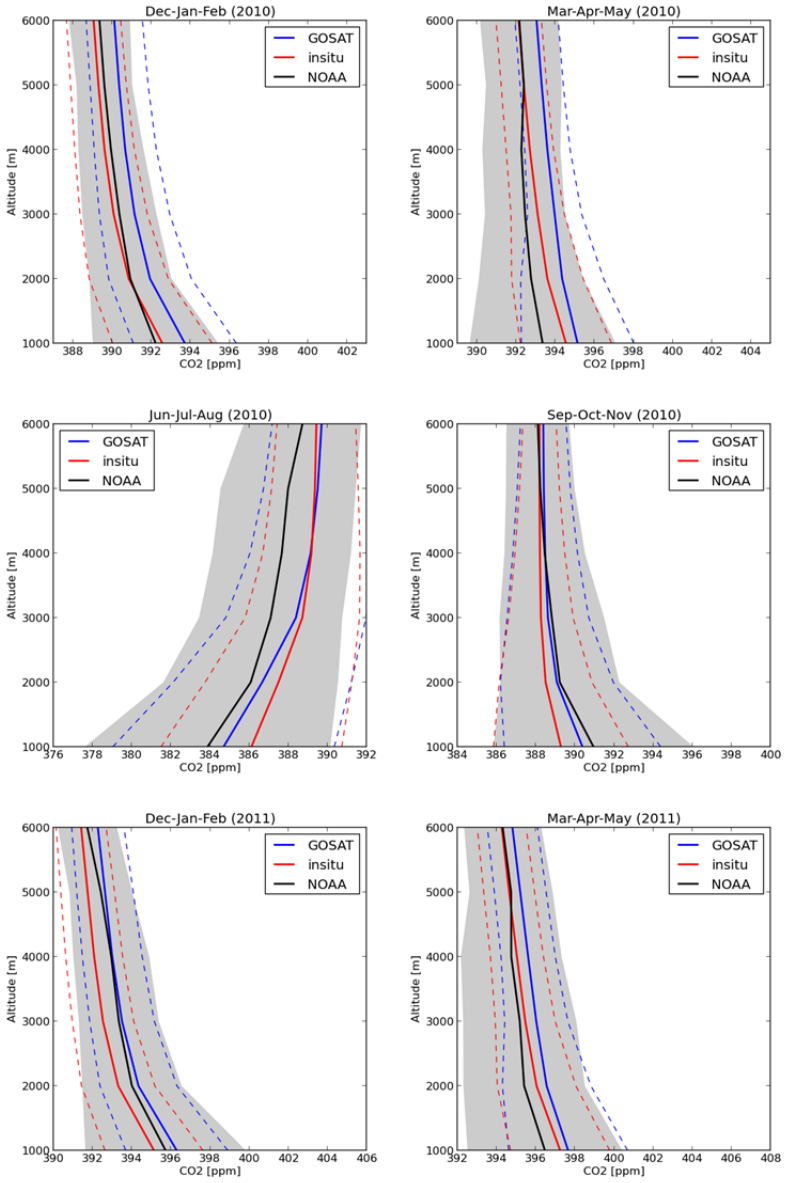

Figure S14. Comparison of mean GEM-MACH-GHG model profiles of CO_2 to NOAA aircraft observations. Observations (black curves) are from obspack_co2_1_PROTOTYPE_v1.0.4_2013-11-25 for locations over continental U.S. and Canada, only. Observed and modelled profiles are binned over 3-month seasons as indicated above each panel. The x-axis of each panel has a range of 16 ppm and ticks of 2 ppm. Model simulations used posterior fluxes from GEOS-Chem inversions with GOSAT (blue) or in situ (red) observations. The shaded grey regions indicate plus or minus one standard deviation for the observations while the dashed coloured lines indicate the same quantities but for the different model runs. Sites used are as in Figures 11cd and S14.

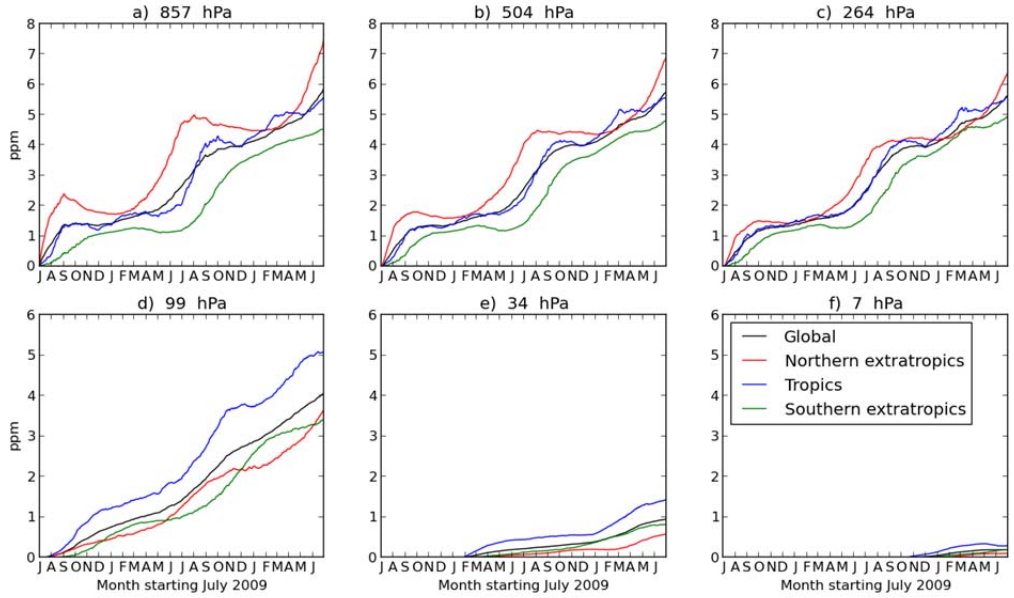

Figure S15. Global mean CO_2 flux signal obtained with GEOS-Chem with in situ-based posterior fluxes. Negative flux signals are shown for the model level closest to the nominal pressure level indicated above each panel. The coloured curves represent the global total (black) and the contributions to this from the various subregions: northern extratropics (red), southern extratropics (green) and tropics (blue). Because the subregions were chosen to have equal areas, 3 times the contribution is depicted so that the mean of the contributions from the subregions gives the total contribution.

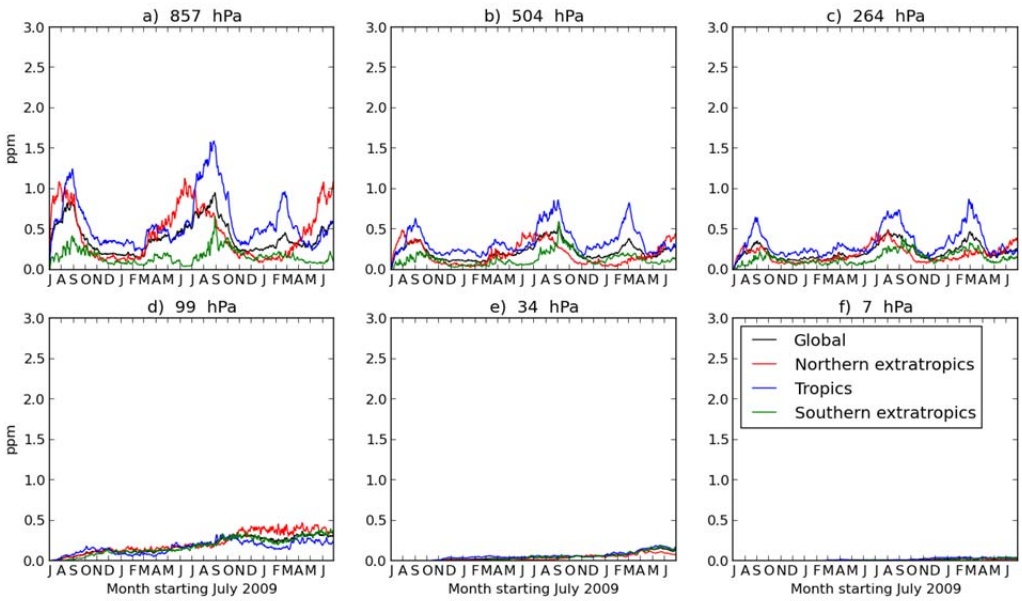

Figure S16. Global mean of zonal standard deviation of the CO_2 flux signal obtained with GEOS-Chem using in situ-based posterior fluxes. Statistics are shown for the model level closest to the nominal pressure level indicated above each panel. The coloured curves represent the global total (black) and the contributions to this from the various subregions: northern extratropics (red), southern extratropics (green) and tropics (blue). Because the subregions were chosen to have equal areas, 3 times the contribution is depicted so that the mean of the contributions from the subregions gives the total contribution.